

Photocatalytic Degradation of 3,3'-Dimethylbiphenyl-4,4'-diamine (*o*-Tolidine) over Nanocrystalline TiO₂ Synthesized by Sol–Gel, Solution Combustion, and Hydrothermal Methods

Praveen K. Surolia, Manoj A. Lazar, Rajesh J. Tayade, and Raksh V. Jasra*

Discipline of Inorganic Materials and Catalysis, Central Salt & Marine Chemicals Research Institute, Council of Scientific and Industrial Research, G. B. Marg, Bhavnagar-364002, India

The nanocrystalline titania catalysts were prepared by sol–gel, solution combustion, and hydrothermal methods. The catalysts were characterized by X-ray diffraction (XRD), Fourier-transform infrared spectrophotometry (FT-IR), scanning electron microscopy (SEM), and BET surface area analysis for their structural properties and by diffuse reflectance spectrophotometer (DRS) for band-gap studies. The photocatalytic activity of synthesized catalysts was determined by the degradation of 3,3'-dimethylbiphenyl-4,4'-diamine (*o*-tolidine). Commercially available P-25 Degussa catalyst was used as a reference catalyst to compare the photocatalytic activity. The percent degradation was determined using UV–visible spectrophotometer, while the mineralization was confirmed by total organic carbon analysis (TOC). A detailed degradation pathway has been suggested based on electrospray ionization mass spectrometry (ESI-MS). Comparison of different catalysts showed that degradation was favored with the sol–gel synthesized TiO₂ catalyst, while mineralization was nearly the same using a catalyst synthesized by sol–gel, solution combustion method, and commercial TiO₂ Degussa P25.

Introduction

The heterogeneous photocatalysis using a semiconductor has been reported to promote the degradation and total mineralization for a wide range of pollutants both from water and air.^{1–5} Titanium dioxide has emerged as an excellent material for the photocatalytic degradation of toxic compounds which are hazardous to health. There are many studies dealing with photocatalytic degradation of organic pollutants from different class of compounds.^{6–11} Most of these studies include a detailed examination of the primary processes of degradation, but provide little information on the reaction mechanism involved in the degradation and identification of major transient intermediates. Also, the literature on the photocatalytic degradation of nitrogen-containing aromatic compounds is sparse.^{12–14}

In all the applications, the morphology, average particle size and size distribution, phase composition, and porosity of titania powders are important factors to be controlled. Nanoparticles show a great tendency to aggregate due to high surface energy combined with their high surface area to volume ratio. This aggregation tendency impedes their use in a variety of applications. For these reasons the synthesis of ultrafine particles with controlled size and surface chemistry is of technological interest. The different synthesis methods are responsible for different characteristics mentioned above. Thus the photocatalytic efficiency depends on the preparation method of the catalyst¹⁵ that can influence significantly the composition and the size of the crystals and the surface distribution of hydroxyl groups.^{16–18} The sol–gel method is a simple and versatile process for the synthesis of nanocrystalline materials. The solution combustion method is a single-step process, and it has been reported that this method gives fine particles/large surface area oxide materials such as alumina, ceria, titania, and zirconia. Micelles and inverse micelles are commonly employed to synthesize TiO₂ nanomaterials.^{19–21}

The aromatics containing nitro and amino groups are toxic in nature^{22–24} and act as an inhibitor for the biodegradation of other compounds of waste.^{25–28} These pollutants enter into the environment during their manufacturing processes and in their use as chemical intermediates in chemical processes. The aromatic amines could cause cyanosis and increased respiratory rate from methemoglobinemia.²⁹ Regardless of exposure route or length, all aromatic amines affect the blood as the primary target organ and need to be stringently controlled.

In the present study, we have synthesized titania samples using different synthesis processes reported earlier^{17,20,21} for the degradation of 3,3'-dimethylbiphenyl-4,4'-diamine (*o*-tolidine). The textural and electronic properties of catalysts were compared using different techniques. Their photocatalytic performance has been compared with a commercial Degussa P25 sample. An attempt was made to correlate structural properties of titanium dioxide to their photocatalytic activity. The mineralization achieved during the reaction was determined by total organic carbon (TOC) analysis. Electrospray ionization mass spectrometry (ESI-MS)^{30,31} technique was used to identify possible major intermediates and photodegradation products, and a possible reaction pathway for mineralization has been suggested.

Experimental

Chemicals and Materials. Titanium dioxide (P25) was purchased from Degussa Corporation (Degussa AG, Frankfurt, Germany). Titanium(IV) tetraisopropoxide (97%) and glycine were procured from Sigma Aldrich, India. *o*-Tolidine (OT), *n*-hexanol and cyclohexane, AR grade, were purchased from E. Merk, India. Deionized distilled water was used to make up the reaction mixture.

Catalyst Preparation. The TiO₂ was synthesized by sol–gel,¹⁷ solution combustion²⁰ and microemulsion mediated hydrothermal synthesis²¹ methods as reported earlier. For sol–gel synthesis procedure, the titanium(IV) tetraisopropoxide was taken with the appropriate amount of dry ethanol in a 500

* To whom correspondence should be addressed. E-mail: rvjasra@gmail.com. Tel.: +91 278 2471793. Fax: +91 278 2567562.

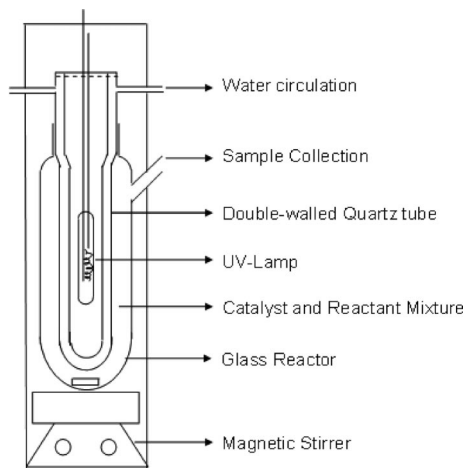


Figure 1. Reactor set up.

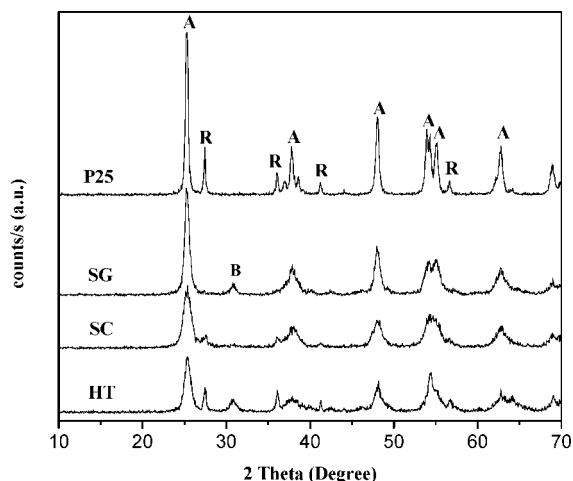


Figure 2. X-ray diffraction pattern for nanocrystalline titania catalysts (A = anatase; R = rutile; B = brookite).

mL round-bottom flask. This mixture was stirred for 30 min (ca. 950 rpm) and then hydrolyzed by controlled drop-by-drop addition of water (1.5 mL min^{-1}). The resulting slurry was peptized for 12 h. The solvent was slowly removed by using a rotavapor (Buchi Rotavapor R-205) at 343 K. The thus obtained sample was further calcined at 723 K for 4 h with a heating rate of $5 \text{ }^{\circ}\text{C min}^{-1}$. The reactant composition was 38 mL of titanium(IV) tetraisopropoxide, 120 mL of dry ethanol, and 160 mL of water. This catalyst prepared was termed as SG.

In solution combustion synthesis, a Pyrex dish (300 cm^3) containing an aqueous redox mixture of stoichiometric amounts of titanium nitrate (2.5 g) and glycine (1.11 g) in 20 mL of distilled water was introduced into a muffle furnace preheated to 623 K. Titanium nitrate was obtained by adding concentrated HNO_3 in to titanium hydroxide, which, in turn, was made by sol-gel method, with stirring and reprecipitated by adding acetone. Inside the furnace, the solution initially undergoes dehydration and a spark appears at one corner which spreads throughout the mass, yielding predominant anatase titania. The glycine acts as a fuel to generate the spark. The thus obtained catalyst was further calcined under similar conditions as mentioned for the sol-gel method. The catalyst thus obtained was termed as SC.

For preparing the microemulsion system, Triton X-100 was used as the surfactant, with *n*-hexanol as cosurfactant and cyclohexane as the continuous oil phase; the solution of tetrabutyl titanate dissolved in acid was employed as the dispersed aqueous phase. The transparent microemulsion was

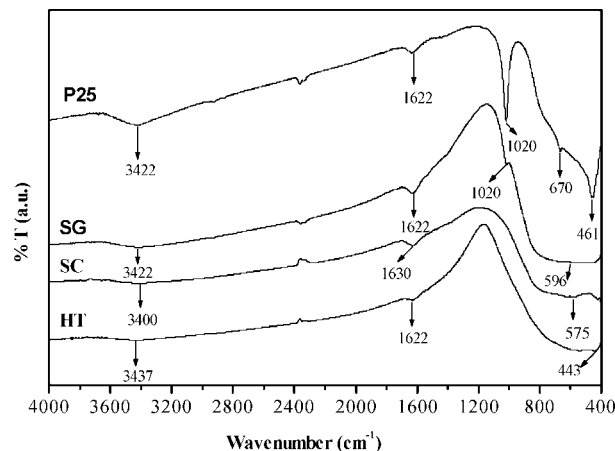


Figure 3. IR spectra of nanocrystalline titania catalysts.

prepared by dispersing the aqueous phase (mixture of 5.4 mL tetrabutyl titanate and 6 mL of 5 M HNO_3) into the Triton X-100/*n*-hexanol/cyclohexane mixture of v/v ratio 5:3:8 with stirring. The stirring was continued for 0.5 h. The transparent feedstock was charged into a 75 mL Teflon-lined stainless autoclave, and the hydrothermal reaction was conducted at 120 $^{\circ}\text{C}$ in an oven for 12 h. The autoclave was cooled to room temperature and the nanocrystalline TiO_2 formed was separated by filtration followed by washing with ethanol and distilled water to remove the oil and surfactant, respectively. The catalyst was dried in air followed by calcination at 723 K at same heating rate applied in sol-gel and solution combustion method for 4 h. The thus obtained catalyst was termed as HT.

Catalyst Characterization. Powder X-ray diffraction patterns were recorded using Cu $\text{K}\alpha_1$ ($\lambda = 0.15405 \text{ nm}$) radiation at 295 K with Phillips X'pert MPD system. Diffraction patterns were taken over 2θ range of 10° – 70° at the scan speed of $0.1^{\circ} \text{ sec}^{-1}$.

The phase content of a sample can be calculated from the integrated intensities of anatase (101), rutile (110), and brookite (121) peaks using the following equations:³²

$$W_A = \frac{K_A A_A}{K_A A_A + A_R + K_B A_B} \quad (1a)$$

$$W_R = \frac{A_R}{K_A A_A + A_R + K_B A_B} \quad (1b)$$

$$W_B = \frac{K_B A_B}{K_A A_A + A_R + K_B A_B} \quad (1c)$$

where W_A , W_R , and W_B , represent the mass fractions of anatase, rutile, and brookite, respectively. A_A , A_R , and A_B are the integrated intensity of the anatase (101), rutile (110), and brookite (121) peaks, respectively. K_A and K_B are two coefficients, and their values are 0.886 and 2.721, respectively.

The crystallite size of Degussa P25 and prepared catalysts were determined from the characteristic peak of $2\theta = 25.3$ (101) for the anatase phase using the Scherrer formula, with a shape³³ factor (K) of 0.9:

$$\text{crystallite size} = K\lambda / (W \cos \theta) \quad (2)$$

where $W = W_b - W_s$, W_b is the broadened profile width of experimental sample, W_s is the standard profile width of reference silicon sample, and λ is the wavelength of X-ray radiation. The crystallinity of the catalysts was calculated with reference to P25 Degussa by taking the average of 5 major

Table 1. Textural and Electronic Properties of Synthesized and Degussa P25 TiO₂ Catalysts

catalyst	anatase ^b (%)	rutile ^b (%)	brookite ^b (%)	average crystallite size ^c (nm)	BET surface area (m ² /g)	pore diameter (nm)	crystallinity ^a (%)	band gap, <i>E_g</i> (eV)
P25	80	20	0	25	54	6,12	100	3.1
SG	83		17	13	80	8	51	3.2
SC	82	18	0	08	95	5	40	3.1
HT	50	21	29	11	78	4	33	3.0

^a Percentage crystallinity was calculated by taking Degussa P25 as 100% crystalline standard. ^b Percentage anatase, rutile, and brookite were calculated by using their relative peak intensity at 2θ values 25.3, 27.4, and 30.8, respectively. ^c Calculated for anatase phase.

anatase peaks of the catalyst ($2\theta = 25.3, 37.7, 47.9, 53.9$, and 55.2).

FT-IR spectroscopic analysis was carried out on a Perkin-Elmer GX spectrophotometer. The spectra were recorded in the range of $400\text{--}4000\text{ cm}^{-1}$ with a resolution of 4 cm^{-1} as KBr pellets. The specific surface area, pore volume, and pore size distribution of the calcined samples were determined from N₂ adsorption-desorption isotherms at 77.4 K using volumetric equation adsorption equipment (ASAP 2010, MicroMetrics, NH), using BET and BJH models.³⁴

The diffuse reflectance spectroscopy (DRS) was used to determine the band-gap energy of the catalysts. The spectra were taken at room temperature in the range of 250–650 nm using a Shimadzu UV-3101PC spectrophotometer. The spectrophotometer was equipped with an integrity sphere^{35,36} and BaSO₄ was used as a reference. Band gap (E_g) = hc/λ was calculated from the minimum of the DRS spectra shown in Figure 55.³⁶

The morphology of all the catalysts was determined with a scanning electron microscope (Leo Series VP1430). The small amount of the samples was dispersed in acetone by ultrasonication. The drop of the dispersed sample was put on a gold-coated aluminum stubs surface. The thus prepared samples were used for scanning electron microscope analysis.

Total organic carbon content (TOC) was measured by using a total organic carbon analyzer (Liqui Toc, Elementar, Germany). Separation of the catalyst particles before TOC analysis was done by filtering the sample solution using a $0.2\text{ }\mu\text{m}$ Millipore membrane filter.

The electro spray ionization mass spectra (ESI-MS) experiments were performed on a Q-TOF micro Y A-260 (Micromass) tandem quadrupole-orthogonal TOF instrument, fitted with a lock spray source using Waters Mass Lynx version 4.0 software. The experiments were conducted with capillary voltage 3071 V, varying the ion energy and collision energy between 1.5–2.0 and 9.5–10.0 V, respectively.

Photocatalytic Activity. Photocatalytic degradation reactions of *o*-tolidine were carried out using a reactor consisting of two parts which was designed and fabricated locally (shown in Figure 1). The first part is the double-wall quartz vessel having an empty chamber at the center.

The irradiation source lamp can be immersed in the chamber. This jacket is facilitated with inlet and outlet for the water circulation to maintain the temperature of reaction mixture. The UV irradiation source used to carry out the reaction was a 125 W mercury vapor lamp (Crompton, high pressure mercury vapor lamp, with the glass bulb removed, radiation wavelength 280–450 nm, photon flux = 0.51 mW cm^{-2}). Spectral distribution of the high pressure mercury vapor lamp given elsewhere.³⁷ The second outer part consists of a borosilicate glass container of a volume of 250 mL after the insertion of inner part. The solution to be degraded was placed in this container.

The photocatalytic activity of catalysts was evaluated by measuring the decrease in concentration of *o*-tolidine in the reaction solution. Prior to commencing illumination, a suspension containing 0.2 g L^{-1} of the catalyst and 250 mL aqueous

solution of ca. 50 ppm of *o*-tolidine was stirred continuously for 30 min in the dark. After attaining the maximum adsorption, the solution was irradiated and the samples (5 mL) were withdrawn by syringe at time intervals of 10 min for the first hour and then once every hour thereafter. The centrifugation was applied to separate out the catalyst from the aqueous samples prior to analysis. The reaction solution was kept homogeneous throughout the reaction by applying continuous stirring using a magnetic stirrer that was below the reactor. The stirring rate was 500 rpm throughout the reaction. All experiments were carried out without the addition of any sacrificial agent. The irradiation source was cooled by circulating water to 293 K during the experiment. The concentration of *o*-tolidine was determined from the absorbance at $\lambda_{\text{max}} = 281\text{ nm}$ using a UV-vis spectrophotometer (Cary 500, Varian, Palo Alto, CA) by calibration curve of *o*-tolidine (concentration vs absorbance) prepared with known concentrations. The tentative fragmentation modes were determined by observing m/z values in mass spectra of the samples at different time intervals during the reaction.

Result and Discussion

Structural Properties. The X-ray diffraction patterns of TiO₂ catalysts are shown in Figure 2. The maximum intense peak at $2\theta = 25.3$ was assigned to the anatase structure, and those at 27.4 were assigned to the rutile of the 101 and 110 plane, respectively. The structural properties of the catalysts are reported in Table 1. All the laboratory synthesized catalysts have an observed smaller crystallite size compared to Degussa P25. As seen in Table 1, the smallest crystallites are obtained from catalyst prepared by the solution combustion method. Crystallinity of all the synthesized catalysts is less than that of the Degussa sample, and the lowest was observed for HT catalysts. The XRD pattern confirms the highest 83% anatase phase of the catalyst SG, while the catalyst HT has a minimum of 50% anatase phase content.

The FT-IR transmission spectra of catalysts produced under different synthesis conditions are shown in Figure 3. The spectra show the band at $400\text{--}600\text{ cm}^{-1}$,^{38,39} including the stretching vibrations of Ti–O bonds at $550\text{--}653\text{ cm}^{-1}$ and Ti–O–Ti bonds at $436\text{--}495\text{ cm}^{-1}$. A broad IR band at the $3400\text{--}3437\text{ cm}^{-1}$ range is due to stretching of –OH groups, and a band at 1020 cm^{-1} which was observed in P25 and SG is attributed to the Ti–OH deformation vibrations. All catalysts have an IR band at the $1622\text{--}1630\text{ cm}^{-1}$ range attributed to deformation vibrations of adsorbed water molecules. An intense band at 1020 cm^{-1} in P25 indicates the presence of a higher amount of surface hydroxyl groups than in the other synthesized TiO₂ catalysts. The difference in the amount of hydroxyl groups may be due to the synthetic route used for the synthesis of nanocrystalline TiO₂.

The specific surface area and average pore diameter reported in Table 1 show that the surface area of Degussa P25, which has the highest crystallites size (25 nm), showed the lowest surface area ($54\text{ m}^2/\text{g}$) and the catalyst prepared by the solution

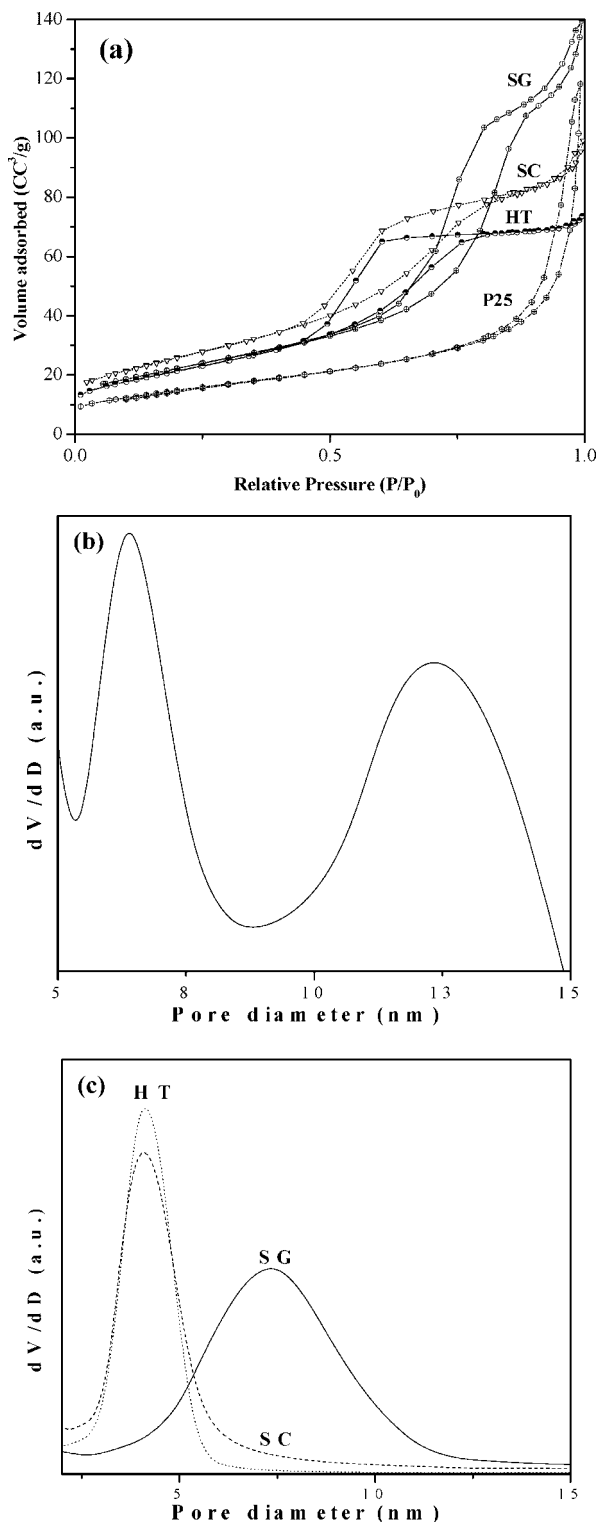


Figure 4. (a) N_2 adsorption/desorption isotherm of the nanocrystalline titania catalysts; BJH pore size distribution plot of (b) Degussa P25 (c) SG, SC, and HT titania catalysts.

combustion method having the smallest crystallites size (8 nm) has a higher specific surface area ($95 \text{ m}^2/\text{g}$). N_2 sorption isotherms for all catalysts are shown in Figure 4a. The laboratory synthesized SG, SC, and HT catalysts have shown type IV behavior with a hysteresis typically observed for mesoporous solids. The BJH desorption pore size distribution determined from the desorption branch of the isotherm is shown in Figure 4b,c. Two types of mesopores are observed in P25, and the hysteresis shown by P25 is slightly different from that of the

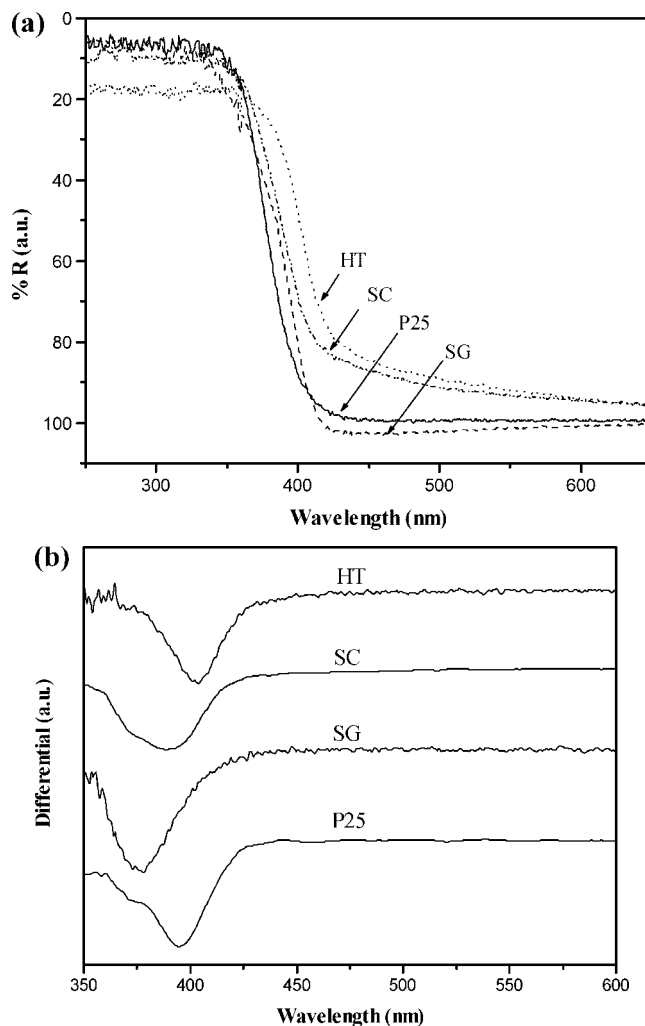


Figure 5. (a) DRS spectra of nanocrystalline titania catalysts; (b) differential spectra of DRS.

other synthesized catalysts. The values of pore diameter are given in Table 1.

DR spectra of the catalysts are shown in Figure 5a. Estimated band-gap values were obtained from the minima in the differential of DR spectra shown in Figure 5b. The band-gap values of all nanocrystalline TiO_2 are in the range of 3.0–3.2 eV. The difference in crystallite size and band gap was attributed to the synthetic route used to prepare the catalysts.

Figure 6 shows the SEM images of all four catalysts. It is evident from the SEM images that synthesized catalysts are spherical particles in morphology in the case of SC and SG, while in case of HT there was no regular shape obtained. The irregularity in the shape of HT may be because of its highly amorphous nature.

Photocatalytic Degradation of *o*-Tolidine in Water by TiO_2 in UV Irradiation. The photocatalytic experiments were performed using TiO_2 Degussa P25 and the laboratory prepared TiO_2 catalysts (SG, SC, and HT) with *o*-tolidine. The catalyst amount used in all cases was 0.2 g/L for a 250 mL of 50 ppm reactant solution, and reaction was carried out up to 4 hours. The amount of adsorption was observed at ca. 18 and 14% with P25 and SG catalysts, respectively, while it was observed only ca. 2 and 4% with SC and HT catalysts, respectively. The initial rate of degradation of *o*-tolidine was higher in the case of SG catalyst as compared to other catalysts. The initial rate of degradation was in the order of $\text{SG} > \text{P25} > \text{SC} > \text{HT}$. The final percentage of degradation was obtained in the range of 82 to

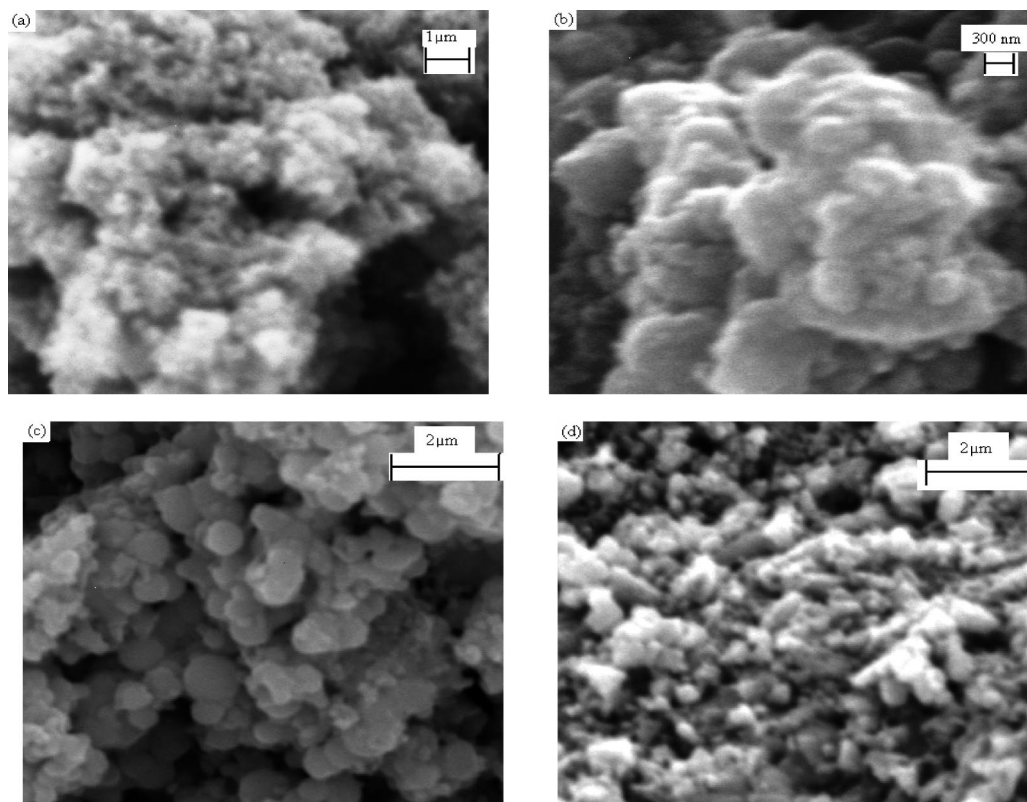


Figure 6. SEM images of (a) P25, (b) SG, (c) SC, and (d) HT catalysts.

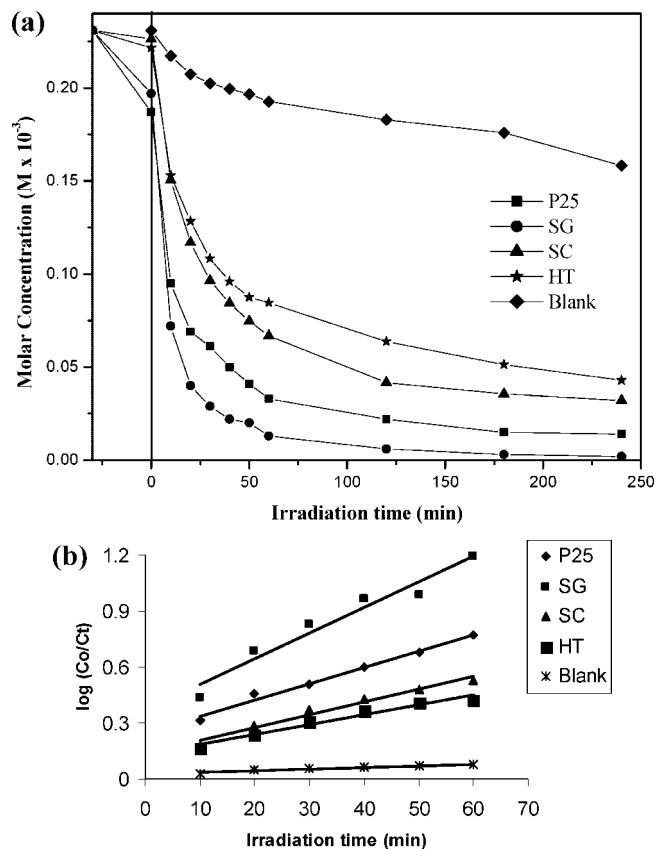


Figure 7. (a) Decrease in concentration of *o*-tolidine as a function of irradiation time; (b) kinetics of *o*-tolidine degradation.

99% after 240 min which was measured by spectrophotometer. The higher percentage of photocatalytic degradation was obtained for SG and P25 catalysts, and it was 99 and 94%,

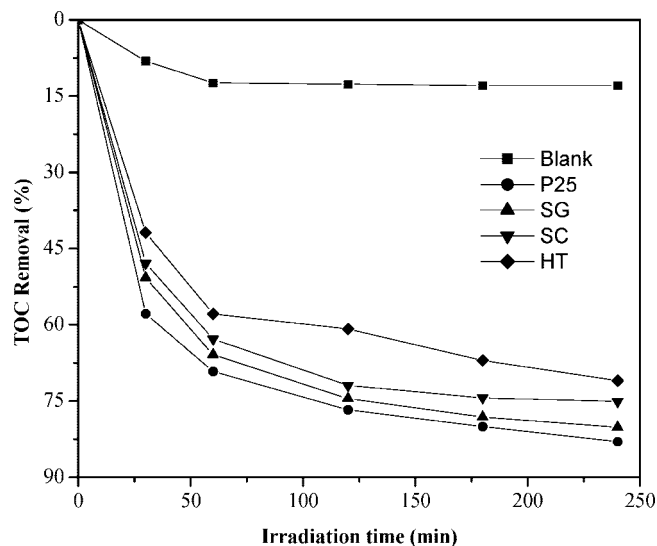


Figure 8. Percent removal of TOC in the photocatalytic degradation of *o*-tolidine

respectively, after 4 hours of reaction. Lowest photocatalytic activity occurred using HT catalyst. The molar concentration values were plotted as a function of duration of UV exposure as shown in Figure 7a. The final percentages, initial rates of degradation, and apparent rate constants are reported in Table 2. The initial rates of degradation of compounds were determined from the initial slope of the concentration profile.

Figure 3 shows that the presence of hydroxyl groups in P25 and SG are higher as compared to those in SC and HT catalysts. The amino functional groups of *o*-tolidine can have some weak interaction with these hydroxyl groups. Figure 4 shows the bimodal nature of pores in P25 with 6 and 12 nm pore diameter, while the surface area of the SG catalyst was attributed to 80

Table 2. Percentage of Degradation and TOC Removal Values and Kinetic Data

catalyst	% degradation ^a (after 240 min)	% TOC removal		initial rate ^a $\times 10^6$ [mol min ⁻¹]	rate constant ^a (k_{app}) $\times 10^2$ [min ⁻¹]	R^2 (degradation)	R^2 (TOC)
		60 min	240 min				
P25	94	69	83	4.5	3.3	0.99	0.93
SG	99	66	80	5.2	5.1	0.96	0.88
SC	86	63	75	4.0	2.3	0.98	0.81
HT	82	58	71	3.6	1.9	0.96	0.90
blank	32	12	16	1.2	0.15	0.95	0.80

^a Calculated using UV–vis absorbance data.

m² g⁻¹ with a pore diameter of 8 nm. This may lead to higher adsorption of *o*-tolidine; 18 and 14% in the case of P-25 and SG catalyst, respectively. The higher adsorption of *o*-tolidine on the P25 and SG catalyst surface increases the probability of attack by radicals formed on the catalyst surface, which results in higher degradation compared to SC and HT catalysts.

A blank study was carried out only in presence of UV light without any catalyst. The concentration of *o*-tolidine was found decreased up to only 32%, using UV–vis spectroscopy.

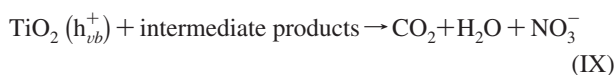
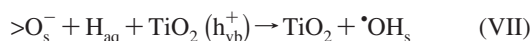
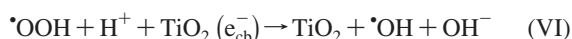
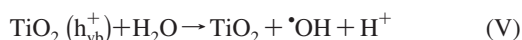
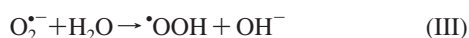
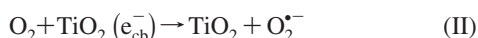
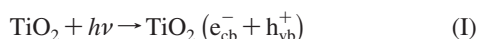
Kinetics of *o*-Tolidine Degradation. The kinetics of *o*-tolidine degradation is represented using Figure 77. This figure shows an adsorption period of 30 min in the dark. It follows pseudo-first-order kinetics in agreement with the Langmuir–Hinshelwood mechanism with the rate r that is proportional to the concentration C_t at any time t ,

$$r = \frac{kKC_t}{1 + KC_t} \approx kKC_t = k_{app}C_t \quad (3)$$

where k is the reaction rate constant and K is the reactant adsorption constant.

The apparent first-order linear transforms are given in Figure 77b. The R^2 values of linearity and apparent rate constants calculated from slopes are given in Table 2. However at the low irradiation time, the reaction was not initiated to follow the linearity shown in Figure 77b, which is due to sharp decrease in concentration which was observed for first 10 min in all the reactions performed. The rate constants represent an index for how fast organic compounds can be converted to intermediates but not necessarily to ultimately CO₂.

Mineralization. Mechanistic explanation of semiconductor photocatalyzed oxidative degradation of organic materials in an aqueous system can be specified by a band-gap model of semiconductors.¹³ A semiconductor is characterized by band structure, that is, a filled valence band (VB) separated by an energy gap (E_g) from a vacant conduction band (CB).



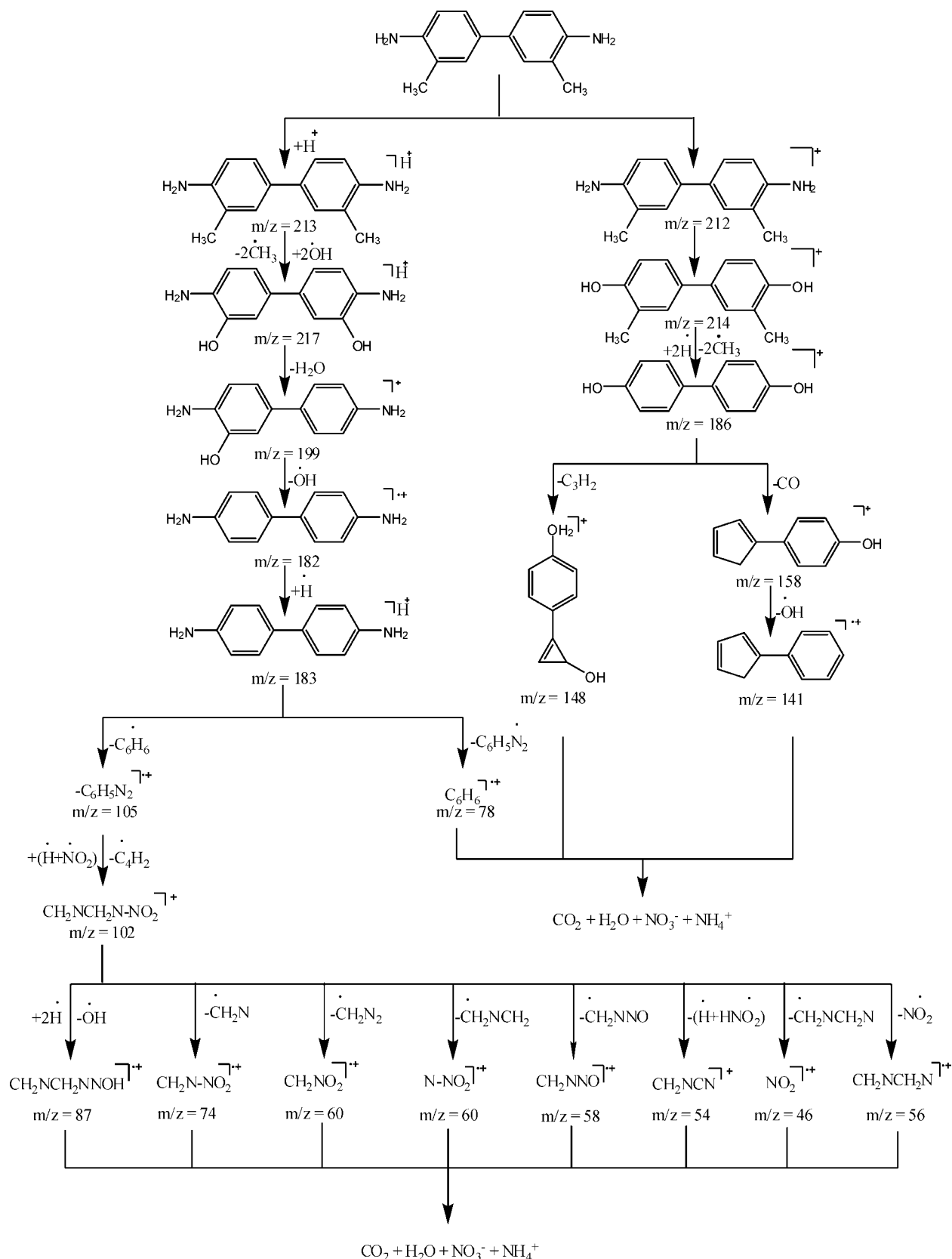
Absorption of a photon with energy equal to or higher than the band gap energy (E_g) promotes an electron from valence band to conduction band, leaving an electron deficiency or hole in the valence band as shown in step I. This e^- and h^+ pair reacts with the surface hydroxyl group or water⁴⁰ and dissolved oxygen to produce hydroxyl, peroxide, and superoxide radical anions as shown in reaction steps II–V. However P. Salvador has proposed that adsorbed hydroxyl groups and water molecules cannot be photooxidized with VB holes.⁴¹ The structural OH^{\bullet} radicals can be photogenerated via electroreduction of OOH^{\bullet} with CB electrons as shown in step VI. The hole generated can react with surface oxygen ions of the TiO₂ lattice at pH below 7 to produce OH^{\bullet} radicals as in step VII. These radicals generated further react with an organic compound, producing a whole range of intermediates including radical and radical cations to achieve complete mineralization, that is, carbon dioxide, water, and inorganic nitrogen with nitrate ion formation.

The mineralization of the reaction mixture was determined by a decrease in TOC values. The mineralization of *o*-tolidine leads to conversion into harmless gaseous CO₂ and inorganic ions such as nitrate and ammonium. The TOC disappearance for the organic molecules is represented in Figure 8 as a function of irradiation time. The R^2 values of the first order kinetics for TOC disappearance are given in Table 2.

The decrease in TOC values was almost the same for SC, SG, and P25 catalyst after 4 h. However Degussa P25 showed a difference in efficiency to some extent compared to all other catalysts including SG catalyst for first hour. The blank study showed only 16% decrease in the TOC value and 32% degradation even after 4 h. The values of percentage degradation and TOC removal confirm that degradation and mineralization are well pronounced in the presence of catalyst.

Characterization of Degradation Products. To study the photocatalytic degradation pathway of *o*-tolidine under irradiation as well as to identify the possible degradation products, ESI-MS was used. For this purpose, mass spectra of the sample taken at different reaction time intervals were observed. Major intermediates during the degradation process are proposed by using m/z values of the mass spectra (Supporting Information). The plausible fragmentation path and intermediates are presented in the scheme 1. The scheme is proposed to start with two different ways. The first path can start with the protonation of the *o*-tolidine parent molecule. The peak at $m/z = 213$ is clearly observed in 30 and 60 min samples. Further removal of methyl radicals followed by hydroxylation may be responsible for the peak at $m/z = 217$. The dehydration and dehydroxylation may provide the m/z values of 199 and 182, respectively.

The second path in Scheme 1 is proposed to start with the formation of the parent molecule cation with m/z value 212. The replacement of amine groups with hydroxyl groups generated during the reaction can form a 3,3'-dimethylbiphenyl-4,4'-diol molecule with an m/z value of 214. Further demethylation gives the peak at $m/z = 186$. These intermediates further reach

Scheme 1. Proposed Fragmentation Pattern of *o*-Tolidine

to mineralization by elimination of various hydrocarbon units, hydroxyl groups and other various possible radicals. The overall mineralization process is multistep and multidirectional which involves various intermediates and radicals formed during the process.

The proposal for 3,3'-dimethylbiphenyl-4,4'-diol formation is feasible in aqueous media because in heterogeneous photocatalysis oxidation by oxidizing species such as hydroxyl and superoxide and reduction by hydrogen radicals are common.

Conclusions

The photocatalytic degradation of *o*-tolidine has been studied using TiO₂ photocatalysts synthesized by sol–gel, solution combustion, and hydrothermal method and compared with commercial P-25 Degussa. The photocatalytic degradation of *o*-tolidine using P-25 and SG catalysts was higher as compared to SC and HT catalysts and mineralization was almost the same using all catalysts. The initial rate of degradation was in the order of SG > P25 > SC > HT. The result showed that the percentage of degradation and mineralization are well pronounced in the presence of catalyst.

Mass spectra at different time intervals of reaction demonstrate the formation of new molecules by the role of radicals formed during the degradation process. These molecules decompose ultimately to achieve complete mineralization, that is, carbon dioxide, water, and inorganic nitrogen which was confirmed by the decreasing TOC values in all the reactions performed.

Acknowledgment

The authors are thankful to the Council of Scientific and Industrial Research, New Delhi, and Dr. P. K. Ghosh, Director of CSMCRI, for the financial assistance and support. The authors are also thankful to Dr. Pragnya Bhatt, Dr. Arun Kumar Das, Mr. Chandrakanth, Mr. Vinod Kumar Agarwal, Mr. Satyaveer Gothwal, Mr. A. P. Sunil, Mr. K. P. Prashanth, and Mr. Renjith Pillai for analytical support.

Supporting Information Available: ESI mass spectra of *o*-tolidine at different time intervals of reaction: (a) original solution, 50 ppm concentration, (b) after 30 min, (c) after 60 min, (d) after 5 h, (e) after 8 h, (f) after 12 h, (g) after 24 h. This material is available free of charge via the Internet at <http://pubs.acs.org>.

Literature Cited

- (1) Hoffmann, M. R.; Martin, S. T.; Choi, W.; Bahnemann, D. W. Environmental Applications of Semiconductor Photocatalysis. *Chem. Rev.* **1995**, *95*, 69–96.
- (2) Fox, M. A.; Dulay, M. T. Heterogeneous Photocatalysis. *Chem. Rev.* **1993**, *93*, 341–357.
- (3) Litter, M. I. Heterogeneous photocatalysis: Transition metal ions in photocatalytic systems. *Appl. Catal., B* **1999**, *23*, 89–114.
- (4) Mills, A.; Hunte, S. L. An overview of semiconductor photocatalysis. *J. Photochem. Photobiol. A* **1997**, *108*, 1–35.
- (5) Balasubramanian, G.; Dionysiou, D. D.; Suidian, M. T.; Subramanian, Y.; Baudin, I.; Laýne', M. Titania powder modified sol-gel process for photocatalytic applications. *J. Mater. Sci.* **2003**, *38*, 823–831.
- (6) Assabane, A.; Ichou, Y. A.; Tahiri, H.; Guillard, C.; Herrmann, J.-M. Photocatalytic degradation of polycarboxylic benzoic acids in UV-irradiated aqueous suspensions of titania. Identification of intermediates and reaction pathway of the photomineralization of trimellitic acid (1,2,4-benzene tricarboxylic acid). *Appl. Catal., B* **2000**, *24*, 71–87.
- (7) Feng, W.; Nansheng, D. Photochemistry of hydrolytic iron (III) species and photoinduced degradation of organic compounds. A minireview. *Chemosphere* **2000**, *41*, 1137–1147.
- (8) Alhakimi, G.; Studnicki, L. H.; Al-Ghazali, M. Photocatalytic destruction of potassium hydrogen phthalate using TiO₂ and sunlight: application for the treatment of industrial wastewater. *J. Photochem. Photobiol. A* **2003**, *154*, 219–228.
- (9) Robert, D.; Dongui, B.; Weber, J.-V. Heterogeneous photocatalytic degradation of 3-nitroacetophenone in TiO₂ aqueous suspension. *J. Photochem. Photobiol. A* **2003**, *156*, 195–200.
- (10) Ao, C. H.; Lee, S. C.; Mak, C. L.; Chan, L. Y. Photodegradation of volatile organic compounds (VOCs) and NO for indoor air purification using TiO₂: promotion versus inhibition effect of NO. *Appl. Catal. B* **2003**, *42*, 119–129.
- (11) Koiminami, H.; Kumamoto, H.; Kera, Y.; Ohtani, B. Photocatalytic decolorization and mineralization of malachite green in an aqueous

suspension of titanium(IV) oxide nanoparticles under aerated conditions: correlation between some physical properties and their photocatalytic activity. *J. Photochem. Photobiol. A* **2003**, *160*, 99–104.

(12) Piccinini, P.; Minero, C.; Vincenti, M.; Pelizzetti, E. Photocatalytic interconversion of nitrogen-containing benzene derivatives. *Faraday Trans.* **1997**, *93*, 1993–2000.

(13) Yang, Y.; Ma, J.; Qin, Q.; Zhai, X. Degradation of nitrobenzene by nano-TiO₂ catalyzed ozonation. *J. Mol. Catal. A* **2007**, *267*, 41–48.

(14) Tayade, R. J.; Surolia, P. K.; Kulkarni, R. G.; Jasra, R. V. Photocatalytic degradation of dyes and organic contaminants in water using nanocrystalline anatase and rutile TiO₂. *Sci. Technol. Adv. Mater.* **2007**, *8*, 455–462.

(15) Sclafani, A.; Palmisano, L.; Schiavello, M. Influence of the preparation methods of titanium dioxide on the photocatalytic degradation of phenol in aqueous dispersion. *J. Phys. Chem.* **1990**, *94*, 829–832.

(16) Oosawa, Y.; Grätzel, M. Effect of surface hydroxyl density on photocatalytic oxygen generation in aqueous TiO₂ suspensions. *J. Chem. Soc., Faraday Trans.* **1988**, *84*, 197–206.

(17) Campostriani, R.; Carturan, G.; Palmisano, L.; Schiavello, M.; Sclafani, A. Sol-gel derived anatase TiO₂: morphology and photoactivity. *Mater. Chem. Phys.* **1994**, *38*, 277–283.

(18) Boonstra, A. M.; Mutsaers, C.A.H.A. Relation between the photoadsorption of oxygen and the number of hydroxyl groups on a titanium dioxide surface. *J. Phys. Chem.* **1975**, *79*, 1694–1698.

(19) Andersson, M.; Osterlund, L.; Ljungstrom, S.; Palmqvist, A. Preparation of Nanosize Anatase and Rutile TiO₂ by Hydrothermal Treatment of Microemulsions and Their Activity for Photocatalytic Wet Oxidation of Phenol. *J. Phys. Chem. B* **2002**, *106*, 10674–10679.

(20) Nagaveni, K.; Sivalingam, G.; Hegde, M. S.; Madras, G. Solar photocatalytic degradation of dyes: high activity of combustion synthesized nano TiO₂. *Appl. Catal. B: Environ.* **2004**, *48*, 83–93.

(21) Wu, M.; Long, J.; Huang, A.; Luo, Y.; Feng, S.; Xu, R. Microemulsion-Mediated Hydrothermal Synthesis and Characterization of Nanosize Rutile and Anatase Particles. *Langmuir* **1999**, *15*, 8822–8825.

(22) Ikeda, S.; Sugiyama, N.; Pal, B.; Marci, G.; Palmisano, L.; Noguchi, H.; Uosaki, K.; Ohtani, B. Photocatalytic activity of transition-metal-loaded titanium(IV) oxide powders suspended in aqueous solutions: Correlation with electron-hole recombination kinetics. *Phys. Chem. Chem. Phys.* **2001**, *3*, 267–273.

(23) Fuente, A.; Hernandez-Alonso, M. D.; Maria, A. J.; Martinez-Arias, A.; Fernandez-Garcia, M.; Conesa, J. C.; Soria, J. Visible light-activated nanosized doped-TiO₂ photocatalysts. *Chem. Commun.* **2001**, *24*, 2718–2719.

(24) Haigler, B. E.; Spain, J. C. Biotransformation of nitrobenzene by bacteria containing toluene degradative pathways. *Appl. Environ. Microbiol.* **1991**, *57*, 3156–3162.

(25) Chou, W. L.; Speece, R. E.; Siddiqi, R. H. Acclimatation and degradation of petrochemical wastewater components by methane fermentation. *Biotechnol. Bioeng. Symp.* **1978**, *8*, 391–414.

(26) Hallas, L. E.; Alexander, M. Microbial Transformation of Nitroaromatic Compounds in Sewage Effluent. *Appl. Environ. Microbiol.* **1983**, *45*, 1234–1241.

(27) Davis, E. M.; Murray, H. E.; Liehr, J. G.; Powers, E. L. Basic microbial degradation rates and chemical byproducts of selected organic compounds. *Water Res.* **1981**, *15*, 1125–1127.

(28) Rodriguez, M.; Timokhin, V.; Michl, F.; Contreras, S.; Gimenez, J.; Esplugas, S. The influence of different irradiation sources on the treatment of nitrobenzene. *Catal. Today* **2002**, *76*, 291–300.

(29) Agency for Toxic Substances and Disease Registry (ATSDR). *Toxicological Profile for nitrobenzene*; U.S. Department of Health and Human Services: Atlanta, GA, 1990. Public Health Service website: <http://www.atsdr.cdc.gov/toxfaqs.html>.

(30) Madeira, P.; Nunes, M. R.; Borges, C.; Costa, F. M. A.; Florêncio, M. H. Benzidine photodegradation: a mass spectrometry and UV spectroscopy combined study. *Rapid Commun. Mass Spectrom.* **2005**, *19*, 2015–2020.

(31) Florêncio, M. H.; Pires, E.; Castro, A. L.; Nunes, M. R.; Borges, C.; Costa, F. M. Photodegradation of Diquat and Paraquat in aqueous solutions by titanium dioxide: evolution of degradation reactions and characterisation of intermediates. *Chemosphere* **2004**, *55*, 345–355.

(32) Yu, J.; Yu, J. C.; Leung, M. K. -P.; Ho, W.; Cheng, B.; Zhao, X.; Zhao, J. Effects of acidic and basic hydrolysis catalysts on the photocatalytic activity and microstructures of bimodal mesoporous titania. *J. Catal.* **2003**, *217*, 69–78.

(33) Cullity, B. D.; Stock, S. R. *Elements of X-ray Diffraction*, 3rd ed.; Prentice Hall Inc.: Upper Saddle River, NJ, 2001.

(34) Gregg, S. J.; Sing, K. S. W. *Adsorption, Surface Area and Porosity*, 2nd ed.; Academic Press: New York, 1982.

(35) Tayade, R. J.; Kulkarni, R. G.; Jasra, R. V. Photocatalytic Degradation of Aqueous Nitrobenzene by Nanocrystalline TiO₂. *Ind. Eng. Chem. Res.* **2006**, *45*, 922–927.

(36) Gratzel, M. *Heterogeneous Photochemical Electron Transfer*; CRC Press: Baton Rouge, LA, 1988.

(37) Tayade, R. J.; Kulkarni, R. G.; Jasra, R. V. Transition Metal Ion Impregnated Mesoporous TiO₂ for Photocatalytic Degradation of Organic Contaminants in Water. *Ind. Eng. Chem. Res.* **2006**, *45*, 5231–5238.

(38) Surolia, P. K.; Tayade, R. J.; Jasra, R. V. Effect of Anions on the Photocatalytic Activity of Fe(III) Salts Impregnated TiO₂. *Ind. Eng. Chem. Res.* **2007**, *46*, 6196–6203.

(39) Kim, E. J.; Hahn, S.-H. Microstructural changes of microemulsion-mediated TiO₂ particles during calcinations. *Mater. Lett.* **2001**, *49*, 244–249.

(40) Poullos, I.; Makri, D.; Prohaska, X. Photocatalytic treatment of olive milling waste water: oxidation of protocatechuic acid. *Global Nest Int. J.* **1999**, *1*, 55–62.

(41) Salvador, P. On the Nature of Photogenerated Radical Species Active in the Oxidative Degradation of Dissolved Pollutants with TiO₂ Aqueous Suspensions: A Revision in the Light of the Electronic Structure of Adsorbed Water. *J. Phys. Chem. C* **2007**, *111*, 17038–17043.

Received for review January 21, 2008

Revised manuscript received May 6, 2008

Accepted May 18, 2008

IE800073J